A finite-element-based approach to quantify the impact of bed joint reinforcement on the compressive strength of vertically perforated clay block masonry

Raphael Suda [a,*], Thomas Kiefer [a], Christian Schranz [b], Josef Füssl [a]

[a] Institute for Mechanics of Materials and Structures, TU Wien, Karlsplatz 13/202, 1040 Vienna, Austria
[b] Digital Building Processes, Institute of Interdisciplinary Construction Process Management, TU Wien, Karlsplatz 13/234, 1040 Vienna, Austria

ABSTRACT

Since lateral tensile stresses trigger failure of vertically perforated clay block masonry under vertical loading, reinforcement of the bed joints introduces a new way to improve the vertical resistance of masonry. The aim of this work is to estimate the feasible increase of the vertical compressive strength by means of the eXtended Finite Element Method (XFEM). Using a unit cell approach and a stochastic strength distribution, the increase of the masonry strength's 5%-quantile could be predicted with 33%. Hence, this work constitutes the vast potential of fibre reinforced bed joints in improving the vertical compressive strength of clay block masonry.

1. Introduction

Being one of the oldest building materials in human history, brick masonry has been used widely, especially in Central Europe. Despite its excellent properties (such as durability, sound protection, energy efficiency, superior indoor climate), masonry lost its dominating role in the building industry, due to the rise of steel and reinforced concrete in the second half of the twentieth century. While innovative research in concrete and steel constructions encouraged the wide usage of these materials, big innovations in optimising the load bearing capabilities of newly built block masonry have not been found. Developments as the use of polyurethane-based glue in the bed joints simplify the construction process, however, the strength of masonry structures is not enhanced, if not even reduced. However, the activity in masonry research has increased again in this field of interest, especially because of the rapid development of computational mechanical methods (see e. g. [1,3,18,21,30,31,34,35,39,42,48]).

Recently, Kiefer et al. [27] proposed a numerical simulation tool to derive the compressive strength of masonry made of vertically perforated clay blocks, as they are widely used for residential low rise buildings in central Europe. The usage of such kind of blocks, laid in thin bed mortar without mortared head joints, results in numerous advantages, as for instance shorter building periods, higher accuracy of construction, and improved masonry properties regarding thermal insulation. However, using this construction technique does not allow for a continuous mortar layer between the blocks, resulting in vertically connected chambers. Especially with installations in the façade and subsequent occurring air circulation, this causes severe problems concerning the airtightness of the building shell. This airtightness is demanded by standards to prevent problems, such as arising mould (e.g. DIN 4108-1 [10]). To encounter this problem, bed joints are occasionally reinforced with fibres, leading to a continuous mortar layer. In the investigated block masonry, failure under vertical compressive loading is triggered by transverse tensile stresses and subsequent occurring cracks. Yet, the fibre reinforcement within the mortar layer increases its stiffness, thereby reducing the tensile stresses in the transverse webs of the block. Since the potential for optimization in changing the block geometry is rather exhausted (see e.g. [8,9,41,49]), reinforcement of the bed joints introduces a new way to improve not only the ductility and horizontal strength (as e.g. Sadek and Lissel [46] already showed), but also the vertical compressive strength of masonry (as e.g. Jasiński and Drobiec [26] suspected for solid autoclaved aerated concrete masonry).

Thus, the main aim of this work is to assess the feasible compressive strength increase due to fibre reinforcement of the bed joints, by

extending the unit cell approach proposed by Kiefer et al. [27], which uses the *eXtended Finite Element Method (XFEM)* combined with the *Virtual Crack Closure Technique (VCCT)* to model the brittle fracture of brick. Another popular modelling approach are *smeared damage models* like regularized damage models or phase field models (see e.g. [12,32,37,43]). While the XFEM introduces discrete cracks in the finite element model, smeared damage approaches are able to model smeared fracture zones by including damage variables in the constitutive model. Especially when facing problems like hard-to-predict initial crack locations, uniting cracks, or dynamic crack growth, classic XFEM poses hard-to-overcome problems. Although different approaches for improving the traditional XFEM tackle these shortcomings (see e.g. [11,52,53]), smeared damage models stay superior in the aforementioned cases. Since the location of cracks could be predicted easily and uniting cracks were not relevant for the problem, using a stable, reliably validated and already available numerical model seemed to be sufficient for reaching this goal.

Building on this model, the outline of the paper can be summarized as follows: First of all, the reinforced mortar joints were introduced by homogenizing the overall stiffness based on a multi-scale material model. Secondly, this modelling strategy was validated by means of compression tests on solid brick pillars, conducted by Trinko et al. [50]. Considering these adaptations, a relation between the amount of reinforcement and the overall strength increase could be developed. Additionally, ten different models with stochastically allocated strength values were generated and numerically evaluated with and without reinforcement. In that way, the effect of strength fluctuations within the clay block could be investigated. These fluctuations are often caused by micro-cracks or material inhomogeneities, originating from the production process.

Finally, a reasonable estimate for the vertical compressive strength increase of clay block masonry due to fibre reinforced bed joints should be provided. Section 2 contains an overview of the applied modelling strategies as well as the validation of these, while Section 3 provides a detailed description of the numerical model. Afterwards, the results are explained and discussed in Section 4, followed by final conclusions to the work in Section 5.

2. Modelling strategies

In the development of new block geometries, manufacturers conduct compressive tests on two different specimen types: single blocks and standardized wall specimens according to EN 1052-1:1998 [15]. The standardized wall specimen is two block lengths wide, five block heights high, and includes mortar joints, thereby reproducing the load transfer mechanisms inside a masonry wall. Due to the difference of these specimens, the obtained compressive strength is significantly smaller when testing a wall specimen than in the single block experiment. This difference originates in the distinct failure mechanisms of both tests.

In the single block experiment the block's top and bottom surface are fully in contact with the steel plates of the testing machine. Therefore, the applied vertical forces induce approximately constant vertical compressive stresses over the block's cross section (see Fig. 1 (a)). Additionally, the friction between the machinery and the specimen disables the lateral deformation of the block's top and bottom faces, leading to lateral compressive stresses close to the top and bottom faces. Conversely, in block masonry under axial compression, as it is represented by the wall specimen, the vertical compressive stresses vary over the block's cross section. While the vertical stresses are approximately constant at half height of each block, transverse webs not standing on top of each other cannot underlie vertical stresses on the top and bottom faces (see Fig. 1 (b)). Hence, the forces have to be redistributed to the load transferring longitudinal webs, yielding tensile stresses on the surface, similar to a plate under vertical loading supported in both lower corners (see Fig. 1 (c)).

There is no way to reliably predict the compressive strength of
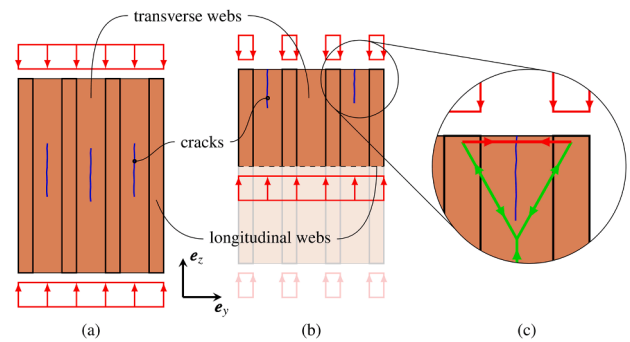

Fig. 1. Differences in load transfer of (a) single block specimen and (b) wall specimen. The truss system in (c) visualizes the load transfer from transverse webs to longitudinal webs (green – compressive force, red – tensile force). The vector e_y is normal to the wall surface. (For interpretation of the references to color in this figure legend, the reader is referred to the web version of this article.)

masonry solely on the single block strength; thus, it is important to consider both block and mortar in the numerical simulation tool. Since the numerical simulation of the whole standardized wall specimen is rather time consuming, Kiefer et al. [27] suggested the usage of a unit cell approach with periodic boundary conditions. This approach enables the simulation of an infinitely large masonry wall, represented through a sufficiently large, characteristic part of the wall. Hence, it was possible to simulate a uniaxial macroscopic stress state, as it can be expected in the middle of the wall specimen, with a model, which was 80% smaller than the real specimen. In combination with Hoffman's orthotropic damage criterion [24] and discrete crack simulation by means of the eXtended Finite Element Method (XFEM), they were able to efficiently predict the vertical compressive strength different block geometries.

2.1. Unit cell with periodic boundary conditions

A masonry wall is here considered as a two-dimensionally periodic structure; bricks (or blocks) and mortar form a constantly repeating pattern. To reduce the computational expense of the numerical simulation, it seems obvious to make use of this structural property. Doing so, it is sufficient to define the mechanical properties solely on a small part of the structure, the so-called *repeating unit cell*, with periodic boundary conditions.

The periodicity of masonry with a lateral block offset of half the block length (see Fig. 2) can be defined by a basis of two linearly independent vectors v_1 and v_2, with the following characteristics: Any point x_b within the structure can be reached by translating a starting point x_a along a vector $m_1 \cdot v_1 + m_2 \cdot v_2$ ($m_1, m_2 \in \mathbb{Z}$). Points x_a and x_b, which are associated in that manner, have the same mechanical properties. The smallest possible unit cell, without considering line or point symmetries, would be the parallelogram spanned by the two vectors v_1
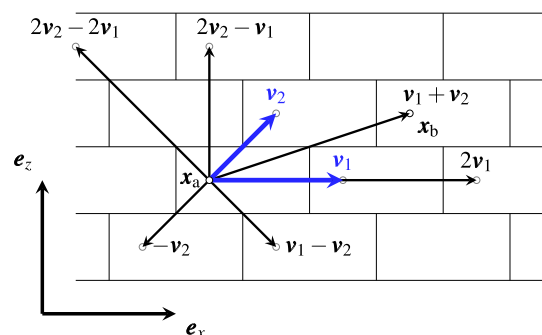
Fig. 2. Two-dimensional periodicity of a common bonding pattern.

and v_2. However, for easily applying the periodic boundary conditions on the FE mesh, it is better to have a cuboid unit cell. Therefore, the extracted section in Fig. 3 was chosen as unit cell. The vectors c_x and c_z describe the unit cell periodicity in directions e_x and e_z, respectively.

Hence, the masonry wall consists of a periodic concatenation of unit cells. Both in undeformed and deformed state, these unit cells have to form a geometrically compatible structure. To satisfy this condition, periodic boundary conditions were formed and applied to the unit cell. These special boundary conditions ensure that two neighbouring faces (thus, opposing faces of a unit cell) deform in the same manner: every point s_k on the unit cell's face has a corresponding point $s_k + c_k$ on the opposing face.

Michel et al. [36] split the strain field $\boldsymbol{\varepsilon}(\boldsymbol{x})$ in a constant part $\langle \boldsymbol{\varepsilon} \rangle$ and a locally fluctuating part $\boldsymbol{\varepsilon}'(\boldsymbol{x})$:

$$\boldsymbol{\varepsilon}(\boldsymbol{x}) = \langle \boldsymbol{\varepsilon} \rangle + \boldsymbol{\varepsilon}'(\boldsymbol{x}), \tag{1}$$

where $\boldsymbol{x}$ marks a point within the unit cell. The constant part of the strain field is defined as mean value over the volume V:

$$\langle \boldsymbol{\varepsilon} \rangle = \frac{1}{|V|} \int_V \boldsymbol{\varepsilon}(\boldsymbol{x}) \mathrm{d}\boldsymbol{x}. \tag{2}$$

Following Eqs. (1) and (2), the local fluctuations have to vanish on average. Integrating Eq. (1) yields to the deformation field $\boldsymbol{u}(\boldsymbol{x})$:

$$\boldsymbol{u}(\boldsymbol{x}) = \langle \boldsymbol{\varepsilon} \rangle \cdot \boldsymbol{x} + \boldsymbol{u}'(\boldsymbol{x}). \tag{3}$$

Each repetition of the unit cell contributes the same deformation $\Delta \boldsymbol{u}$ to the overall deformation. This deformation can be calculated for each pair of corresponding points, by means of Eq. (3):

$$\Delta \boldsymbol{u}_k = \boldsymbol{u}(\boldsymbol{s}_k + \boldsymbol{c}_k) - \boldsymbol{u}(\boldsymbol{s}_k) = \langle \boldsymbol{\varepsilon} \rangle \cdot \boldsymbol{c}_k. \tag{4}$$

Since $\langle \boldsymbol{\varepsilon} \rangle$ and $\boldsymbol{c}_k$ are constant within the unit cell, the deformation difference of two in direction k opposing faces, $\Delta \boldsymbol{u}_k$, has to be constant too. This property enables the definition of so-called master vertices; the deformation of those master vertices defines the deformation state on the boundary of the unit cell.

Fig. 4 shows a reasonable name convention for cuboid unit cells, proposed by Böhm [5]. Hereby, faces are labelled *N*, *S*, *E*, *W*, *T*, and *B* (*North*, *South*, *East*, *West*, *Top*, and *Bottom*, respectively), while names of edges and vertices consist of the labels of the intersecting faces (eg. SE for a edge and SWB for a vertex).

The chosen unit cell is periodic in *x*- and *z*-direction, the *y*-axis is rectangular to the wall surface. Therefore, the faces *East* and *West* are coupled, as well as *Top* and *Bottom*, while *South* and *North* may deform freely. Although this paper only considers strictly vertical loading, the following periodic boundary conditions include the implementation of
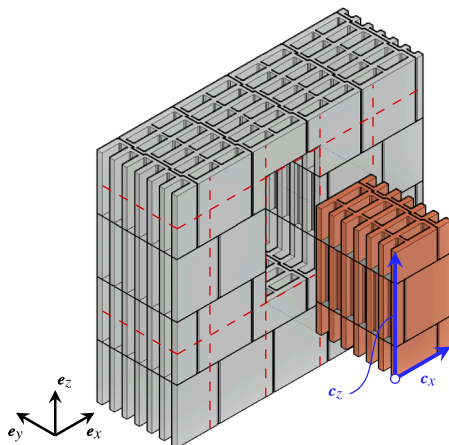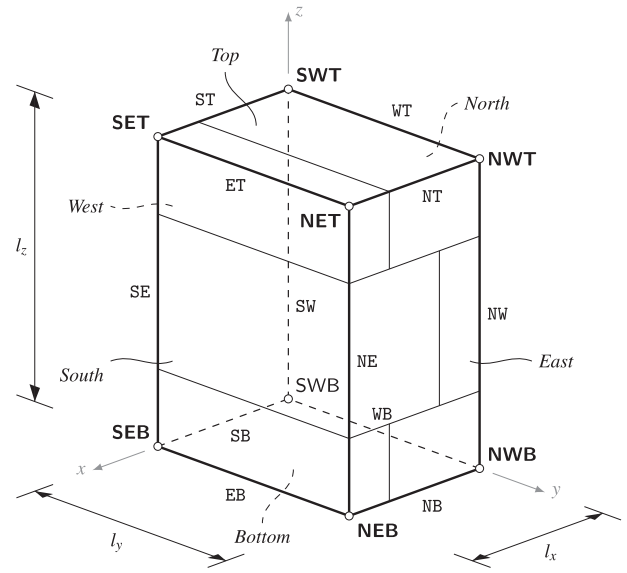

Fig. 4. Name convention for the faces, edges and vertices of a three-dimensional cuboid unit cell.

more general deformation states. Considering the translation of the edges WB and WT, the displacements in *x*- and *z*-direction are the following on each point on face *Bottom* (see Fig. 5):

$$\begin{pmatrix} u_x^B(y) \\ u_z^B(y) \end{pmatrix} = \begin{pmatrix} u_x^{SWB} \\ u_z^{SWB} \end{pmatrix} + \frac{y}{l_y} \cdot \begin{pmatrix} u_x^{NWB} - u_x^{SWB} \\ u_z^{NWB} - u_z^{SWB} \end{pmatrix}. \tag{5}$$

The same relation applies on face *Top*:

$$\begin{pmatrix} u_x^T(y) \\ u_z^T(y) \end{pmatrix} = \begin{pmatrix} u_x^{SWT} \\ u_z^{SWT} \end{pmatrix} + \frac{y}{l_y} \cdot \begin{pmatrix} u_x^{NWT} - u_x^{SWT} \\ u_z^{NWT} - u_z^{SWT} \end{pmatrix}. \tag{6}$$

Since u_x^{SWB} and u_x^{NWB} are not necessarily equal, rotations may occur, which result in displacements along the *y*-axis, u_y (see Fig. 5):
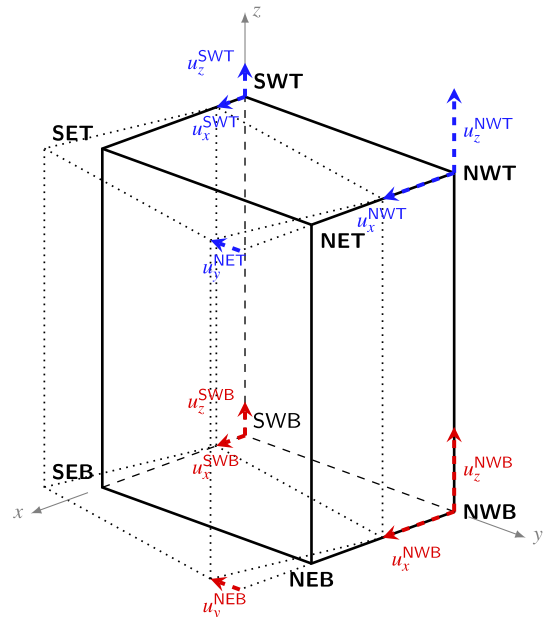

Fig. 5. Translation and rotation of face *West* due to displacements of master nodes.

Fig. 3. Chosen unit cell.

$$u_y^B(x) = u_y^{SWB} - \frac{x}{l_y} \cdot \left(u_x^{NWB} - u_x^{SWB}\right) \quad \text{and} \tag{7}$$

$$u_y^T(x) = u_y^{SWT} - \frac{x}{l_y} \cdot \left(u_x^{NWT} - u_x^{SWT}\right). \tag{8}$$

Joining Eqs. (5)–(8) results in the coupling of the faces *Top* and *Bottom*:

$$\Delta u_z = \begin{pmatrix} u_x^T(x,y) - u_x^B(x,y) \\ u_y^T(x,y) - u_y^B(x,y) \\ u_z^T(x,y) - u_z^B(x,y) \end{pmatrix} = \begin{pmatrix} u_x^{SWT} - u_x^{SWB} \\ u_y^{SWT} - u_y^{SWB} \\ u_z^{SWT} - u_z^{SWB} \end{pmatrix}$$

$$+ \begin{pmatrix} \frac{y}{l_y} \cdot \left(\left(u_x^{NWT} - u_x^{SWT}\right) - \left(u_x^{NWB} - u_x^{SWB}\right)\right) \\ -\frac{x}{l_y} \cdot \left(\left(u_x^{NWT} - u_x^{SWT}\right) - \left(u_x^{NWB} - u_x^{SWB}\right)\right) \\ \frac{y}{l_y} \cdot \left(\left(u_z^{NWT} - u_z^{SWT}\right) - \left(u_z^{NWB} - u_z^{SWB}\right)\right) \end{pmatrix}. \tag{9}$$

Formulating the deformations for the edges WB and EB in an analogous manner results in the coupling of the faces *East* and *West*:

$$\Delta u_x = \begin{pmatrix} u_x^E(y,z) - u_x^W(y,z) \\ u_y^E(y,z) - u_y^W(y,z) \\ u_z^E(y,z) - u_z^W(y,z) \end{pmatrix} = \begin{pmatrix} u_x^{SEB} - u_x^{SWB} \\ u_y^{SEB} - u_y^{SWB} \\ u_z^{SEB} - u_z^{SWB} \end{pmatrix}$$

$$+ \begin{pmatrix} \frac{y}{l_y} \cdot \left(\left(u_x^{NEB} - u_x^{SEB}\right) - \left(u_x^{NWB} - u_x^{SWB}\right)\right) \\ -\frac{z}{l_y} \cdot \left(\left(u_z^{NEB} - u_z^{SEB}\right) - \left(u_z^{NWB} - u_z^{SWB}\right)\right) \\ \frac{y}{l_y} \cdot \left(\left(u_z^{NEB} - u_z^{SEB}\right) - \left(u_z^{NWB} - u_z^{SWB}\right)\right) \end{pmatrix}. \tag{10}$$

The linear Eqs. (9) and (10) were applied to each pair of corresponding nodes to ensure the geometrical compatibility of the unit cell in any loading scenario. Both free surfaces *Top* and *Bottom* may deform freely; thus, the stresses on those surfaces have to equal zero. Hence, merely the deformations of six out of eight vertices are needed to fully define the boundary conditions. Therefore, these vertices, SWT, NWT, SWB, NWB, SEB, and NEB, are designated master nodes. To simulate a specific loading scenario, deformations were applied on the master nodes, following Eq. (4). A pure vertical loading is applied by specifying the constant strain in z-direction, $\langle \varepsilon_{zz} \rangle$, to nonzero, while setting each other constant strain component to zero:

$$\Delta u_x = \langle \boldsymbol{\varepsilon} \rangle \cdot c_x = \begin{pmatrix} 0 \\ 0 \\ 0 \end{pmatrix}, \ \Delta u_z = \langle \boldsymbol{\varepsilon} \rangle \cdot c_z = \begin{pmatrix} 0 \\ 0 \\ \langle \varepsilon_{zz} \rangle \cdot l_z \end{pmatrix}. \tag{11}$$

Excluding rigid body translations and rotations, the periodic boundary conditions (Eqs. (9) and (10)) only fulfil these constraints by setting the vertical displacements of the vertices NWT and SWT to $\langle \varepsilon_{zz} \rangle \cdot l_z$ and the remaining displacements to zero (see Fig. 6).

2.2. Brittle failure of fired clay

Extruded bricks show a distinct orthotropic material behaviour, caused by the production process. When the raw mixture is being extruded, the flat clay minerals align parallel to the extrusion direction, as Bourret et al. [7] showed. The highest stiffness and strength values are oriented in extrusion direction, while the values in perpendicular
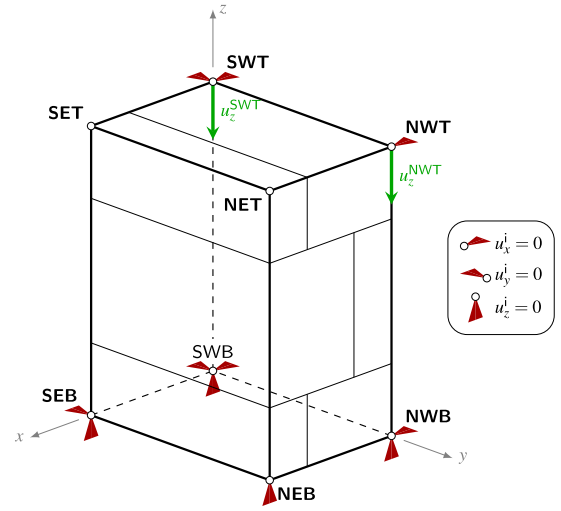

Fig. 6. Applied deformations on the unit cell.

direction may be significantly smaller. This orthotropy especially occurs in vertically perforated clay blocks with thin webs. Fig. 7 shows the varying local coordinate systems over the block's cross section. While the local Z-axis is always parallel to the global z-axis (the extrusion direction), the orientation of the L- and T-axis depends on the location within the block geometry. The L-axis (longitudinal) is parallel to the longer side of each part; the T-axis (transversal) is rectangular to the L-axis. Capital letters are used for the local coordinates (L, T, Z), whereas lower case letters indicate global coordinates (x, y, z). Two different types of webs may be distinguished due to the geometry of the vertical perforations: *longitudinal webs* are aligned lengthwise with the wall, *transverse webs* are oriented rectangular to the wall surface.

Cracking processes are a central matter in the failure of brittle materials like fired clay. Those cracks are always attended with high gradients in the stress field near the crack tip. Thus, the mesh would have to be refined around the crack tip. Consequently, the mesh has to be continually updated when simulating propagating cracks. The eXtended Finite Element Method (XFEM), introduced by Belytschko and Black [2], allows the modelling of discrete propagating cracks without remeshing. Based on the partition of unity finite element method of Melenk and Babuška [33], the elements are being subdivided into parts, on which different shape functions are applied. This partition enables the local enrichment of the nodal degrees of freedom with special displacement functions:

$$u(x) \approx \sum_i^{NN} N_i(x) \cdot \left[u_i + H_i(x) \cdot a_i + \sum_j G_j(x) \cdot b_{ij} \right], \tag{12}$$
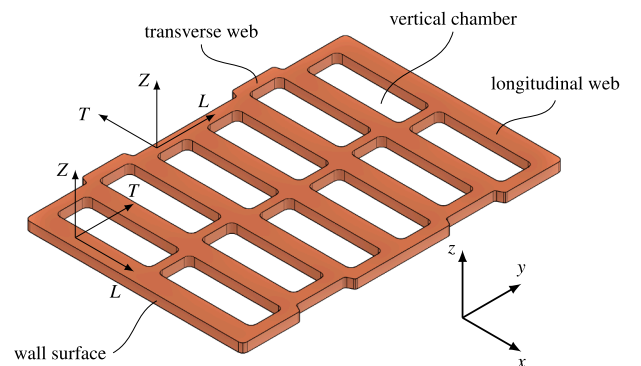

Fig. 7. Parts of a vertically perforated clay block and local coordinates for describing the material properties.

where N_i are the used nodal shape functions, u_i the nodal displacements, H_i the nodal enrichment functions, G_j the crack tip functions, and a_i as well as b_{ij} the additional degrees of freedom for totally and partly cracked elements. While the first term in square brackets of Eq. (12) describes the approximation of the displacement field for the uncracked regions, the second and third part apply for fully and partly cracked elements, respectively. The numerical simulation tool was modelled in the commercial FE software *Abaqus*, in which the crack tip functions are not considered. Since these functions depict the high stress gradients near the crack tip, the used approach is more sensitive to the chosen mesh. Being fully aware of this fact, the chosen meshes were sufficiently refined where needed.

For describing the location and geometry of cracks, the so-called level-set method is applied [19,38]. The two level-set functions $\phi(x)$ and $\psi(x)$ are able to describe the location of a crack, relative to a given position x. The function $\phi(x)$ specifies the orthogonal distance of the point x to the crack surface, while $\psi(x)$ denotes the distance to the crack tip. With these two functions, the crack geometry may be described, whereas

$$\phi(x) = 0, \psi(x) < 0 \qquad \text{defines the crack surface,} \qquad (13)$$

$$\phi(x) = 0, \psi(x) = 0 \qquad \text{defines the crack tip, and} \qquad (14)$$

$$\psi(x) > 0 \qquad \text{is not located on the crack at all.} \qquad (15)$$

Abaqus uses the modified Heaviside function $H(x)$ [38] as the nodal enrichment function:

$$H_i(x) = H(\phi(x)) = \begin{cases} -1 & \text{for } \phi(x) < 0 \\ +1 & \text{for } \phi(x) \geqslant 0 \end{cases}. \qquad (16)$$

The level-set for the crack surface, $\phi(x)$, is directly used as the argument for the enrichment function.

Two different components are necessary for the modelling of propagating cracks with the FEM:

1. a **damage initiation criterion** $f(\sigma)$ to indicate failure within an element, and
2. a **damage evolution criterion** to define the ductility and therefore the propagation rate of the crack.

When the damage initiation criterion indicates failure, the affected element is being partitioned along a plane surface, given by the maximum plain stress, but **not yet** split. Those partitions stay bonded until the damage evolution criterion is fulfilled. Within the present work, a combination of Hoffman's orthotropic failure criterion [24] with the Virtual Crack Closure Technique (VCCT) was used.

2.2.1. Crack initiation with the orthotropic Hoffman criterion

Graubner and Richter [18] studied different failure criteria for the numerical simulation of brick and found the Hoffman criterion [24] to be suitable for modelling brick failure. The criterion uses each component of the stress tensor σ and is capable of indicating failure under tensile as well as combined stress states. Triaxial compression failure cannot be depicted with the Hoffman criterion. Since the main reason of failure are tensile stresses in the transverse webs, this lack of coverage is acceptable for the present work. Anyhow, Kiefer et al. [27] have shown that even a simple principal stress criterion yields reasonable results, which confirms the assumption of lateral tensile stresses governing the failure mechanism.

Mathematically, Hoffman's failure criterion reads as follows:

$$\begin{aligned} f(\sigma) \quad &= C_1 \cdot (\sigma_{TT} - \sigma_{ZZ})^2 + C_2 \cdot (\sigma_{ZZ} - \sigma_{LL})^2 \\ &+ C_3 \cdot (\sigma_{LL} - \sigma_{TT})^2 \\ &+ C_4 \cdot \sigma_{LL} + C_5 \cdot \sigma_{TT} + C_6 \cdot \sigma_{ZZ} \\ &+ C_7 \cdot (\sigma_{LT})^2 + C_8 \cdot (\sigma_{TZ})^2 + C_9 \cdot (\sigma_{LZ})^2, \end{aligned} \qquad (17)$$

with the components of the stress tensor, σ_{ij}, and the constant parameters C_1 to C_9 depending on the materials tensile, compressive, and shear strengths, $\sigma_{t,i}$, $\sigma_{c,i}$, and $\sigma_{s,ij}$, respectively:

$$C_1 = \frac{1}{2} \left[\left(\sigma_{t,T} \cdot \sigma_{c,T} \right)^{-1} + \left(\sigma_{t,Z} \cdot \sigma_{c,Z} \right)^{-1} - \left(\sigma_{t,L} \cdot \sigma_{c,L} \right)^{-1} \right],$$
$$C_2 \text{ and } C_3 \text{ by permutation of indices } L, T, Z, \qquad (18)$$

$$C_4 = \left(\sigma_{t,L} \right)^{-1} - \left(\sigma_{c,L} \right)^{-1},$$
$$C_5 \text{ and } C_6 \text{ by permutation of indices } L, T, Z, \qquad (19)$$

$$C_7 = \left(\sigma_{s,TZ} \right)^{-2},$$
$$C_8 \text{ and } C_9 \text{ by permutation of indices } L, T, Z. \qquad (20)$$

While tensile and compressive strengths are available from experiments (see Section 3.2), the shear strengths could only be estimated. Graubner and Richter [18] obtained reasonable results by assuming the shear strengths between the mean value of the corresponding tensile strengths and half of the mean value of the corresponding compressive strengths:

$$\tau_{ij,\min} = \frac{\sigma_{t,i} + \sigma_{t,j}}{2}, \qquad \tau_{ij,\max} = \frac{\sigma_{c,i} + \sigma_{c,j}}{4}. \qquad (21)$$

In the present work, the shear strengths were specified as mean value of those boundaries.

2.2.2. Crack propagation with the Virtual Crack Closure Technique

The brittle material behaviour of fired clay can be described accurately by means of linear elastic fracture mechanics, which forms the basis for the application of the Virtual Crack Closure Technique. The main assumption of this technique is the following: The released strain energy due to opening of a crack is equal to the energy, required for closing the same crack. Based on this assumption, the energy release rate G is calculated and compared with the critical energy release rate G_c, which is a material property. As soon as the energy release rate exceeds the critical value, the crack extends. In the present work, the crack propagation criterion was defined to consider all three failure modes by means of a power law (as it is implemented in *Abaqus*):

$$f = \frac{G}{G_c} = \left(\frac{G_I}{G_{I,c}} \right)^a + \left(\frac{G_{II}}{G_{II,c}} \right)^b + \left(\frac{G_{III}}{G_{III,c}} \right)^c = 1. \qquad (22)$$

Hereby, the energy release rate is calculated and compared to the critical energy release rate for each failure mode separately. Additionally, the superscripts a, b and c affect the interaction between the failure modes.

Kiefer et al. [27] assigned 0.025 J/mm^2 to the critical energy release rate for mode-I failure, $G_{I,c}$. These values where chosen after Eis and Vassilev [14], who did three-point bending tests on different brick specimen and back-calculated the fracture energy via a genetic algorithm proposed by Hannawald [22]. Bocca et al. [6] determined similar fracture energy values from three-point bending tests and achieved good results recalculating the experiments with a cohesive crack model considering linear elastic fracture mechanics. While critical energy release rates for mode-I failure are already scarce in literature, data for mode II and mode III are even harder to find. However, since [27] showed that the tensile stresses govern failure of vertically perforated clay block masonry, mode I is the decisive failure mode. Therefore, the values $G_{II,c}$ and $G_{III,c}$ have to be distinctly higher, for example $G_{II,c}/G_{I,c} = G_{III,c}/G_{I,c} = 10$, as proposed by [27] Considering this ratio, $G_{II,c}$ and $G_{III,c}$ were set to 0.25 J/mm^2, assuming linear interaction the coefficients a, b and c were all set to 1.

2.3. Mortar bed joint

The considered vertically perforated clay blocks are usually used with thin bed mortar as bed joint. In general those mortars consist of

cement, chalk, and sand or quartz sand powder. Thin bed mortar behaves similarly to concrete without reinforcement: strengths and Young's modulus are isotropic, the mortar basically deforms linear elastic and fails brittle under tensile stresses without distinct plastic behaviour. While the compressive strength of different thin bed mortars are fairly high, the tensile stresses stay rather low in comparison.

Due to the hydraulic solidification of cement mortar, the material properties strongly depend on the amount of available water. For a complete hydratation of the mortar, a water-cement ratio around 0.4 is ideal – the weight of available water should be 0.4 times the cement's weight. Since fired clay tends to absorb significant amounts of the water bound to the mortar, manufacturers adjust their mortars to their range of products; in the mixing instruction a water amount is specified, which takes the absorption behaviour of the fired clay into account. The compressive strength obtained from experiments on mortar specimens is therefore smaller than the compressive strength of the same mortar as part of the masonry.

Within this work, the mortars material behaviour was considered linear elastic and isotropic. Mortar failure was assumed to be insignificant for the vertical compressive strength of the numerical model. This assumption is based on the following reasons:

- The (already high) compressive strength obtained from tests on mortar cubes increases further in the masonry due to the absorption behaviour of the fired clay.
- In those regions of the reinforced mortar joint, which are not located on top of a web, tensile stresses occur. Additionally, shrinkage yields small cracks. Those regions are therefore considered as cracked within the model; accordingly, solely the stiffness of the glass fibre mesh is considered there (see Section 3.3).

2.3.1. Reinforced mortar with homogenized stiffness

To encounter the aforementioned problems regarding airtightness using vertically perforated clay block masonry, a glass fibre mesh is occasionally embedded in the mortar bed joints. Failure of the masonry is induced by lateral tensile stresses in the webs due to transverse webs being not on top of each other. The fibre mesh within the mortar joint increases its overall stiffness, thereby reducing the tensile stresses in the transverse webs of the block. Glass fibres have a rather high Young's modulus and tensile strength, compared to common mortars (see Table 1).

The mesh was assumed to be fully embedded in mortar, lying midmost in the bed joint (see Fig. 8). Discretely modelling each glass fibre would be inefficient; not only the modelling of each single fibre would have been time consuming (especially when modelling different ratios of reinforcement!), also the computational expense would increase heavily. Instead, the reinforced Mortar joint was considered as a homogenized layer within the model; the homogenized material parameters were obtained from a multiscale model. Therefore, only the materials' stiffness tensors $\mathbb{C}_i$, the volume fractions of the components on the entire layer, f_i, and information about the fibre's orientation were needed.

The homogenization was conducted on a representative part of the layer, the so-called *representative volume element* (RVE, see Fig. 8). For reasonably defining an RVE, the *separation of scales* must be fulfilled:

$$d \overset{\sim 1.5-3}{\ll} l \underset{\sim 5-10}{\ll} \mathscr{L}, \tag{23}$$

Table 1
Glass fibre properties compared to thin bed mortar [17,25].

	glass fibre	mortar
Young's modulus E	80000 MPa	5000 MPa
Tensile strength σ_t	2000 MPa	7.7 MPa
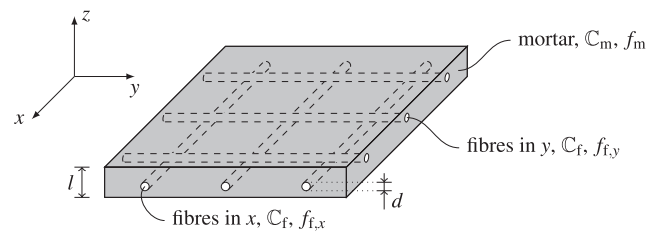
Fig. 8. Representative volume element (RVE).

meaning that the characteristic length of the RVE, l, has to be at least one and a half to three times bigger than the characteristic size of the inhomogeneities, d, [13,44] and at least five to ten times smaller than the characteristic length scale of the loading, $\mathscr{L}$ [28]. With this requirement fulfilled, the strains and stresses on the macroscopic scale (on the edges of the RVE), $\boldsymbol{\varepsilon}^M$ and $\boldsymbol{\sigma}^M$, respectively, may be calculated from the microscopic stresses and strains, $\boldsymbol{\varepsilon}^\mu$ and $\boldsymbol{\sigma}^\mu$, in the following way:

$$\boldsymbol{\varepsilon}^M = \langle \boldsymbol{\varepsilon}^\mu(\boldsymbol{x}^\mu) \rangle, \qquad \boldsymbol{\sigma}^M = \langle \boldsymbol{\sigma}^\mu(\boldsymbol{x}^\mu) \rangle, \tag{24}$$

where $\langle . \rangle$ is defined as the average over the RVE's volume, similar to the definition in Eq. (2).

The microstructure consists of different regions with quasi-homogeneous properties – the so-called material phases. In this case, the material phases are mortar and glass fibres. Each of those phases r occupies a volume V_r^μ, and therefore has a volume fraction f_r^μ on the entire volume V_{RVE}:

$$f_r^\mu = \frac{V_r^\mu}{V_{RVE}}, \qquad \sum_{r=1}^{N_r} f_r^\mu = 1, \tag{25}$$

where N_r is the total number of material phases. With these volume fractions defined, the homogenization scheme in Eq. (24) simplifies to the following discrete scheme:

$$\boldsymbol{\varepsilon}^M = \sum_{r=1}^{N_r} f_r^\mu \cdot \boldsymbol{\varepsilon}_r^\mu(\boldsymbol{x}^\mu), \quad \boldsymbol{\sigma}^M = \sum_{r=1}^{N_r} f_r^\mu \cdot \boldsymbol{\sigma}_r^\mu(\boldsymbol{x}^\mu) \tag{26}$$

The homogenized stiffness tensor $\mathbb{C}^M$ is then calculated as follows:

$$\mathbb{C}^M = \sum_{r=1}^{N_r} f_r^\mu \cdot \mathbb{C}_r^\mu : \mathbb{A}_r^\mu, \tag{27}$$

with each phase's stiffness tensor $\mathbb{C}_r^\mu$ and concentration tensor $\mathbb{A}_r^\mu$.

Eshelby [16] and Laws [29] provided an approach to calculate these concentration tensors, which only requires the knowledge of the inclusions' shape additionally to the phases' stiffness tensors. The glass fibres were considered as cylindrical inclusions in two orthogonal directions (see Fig. 8); the Mori-Tanaka-scheme [40] was used for solving the homogenization problem.

2.4. Surface interaction between brick and mortar

The contact properties between brick and mortar play a major role in the interaction of both materials. Hereby, the shear strength τ_u depends on the present axial (compressive) stress in the joint. Van der Pluijm [45] proposes a relation, based on Coulomb's friction law:

$$\tau_u = c_0 - \tan(\varphi) \cdot \sigma_n, \tag{28}$$

with the shear bond strength c_0, the angle of internal friction φ, and the axial compressive strength σ_n. As long as the shear stresses on the interface remain sufficiently small, the bonding of brick and mortar stays intact. Hence, the interface is modelled as being tied. To check out the validity of this clearly strong simplification, the shear stresses on the interface were monitored throughout the simulations.

2.5. Stochastic allocation of material strengths to the webs

Calculations with homogeneous material properties showed that without reinforcement the first crack was critical for the failure. When exceeding a certain amount of reinforcement, additional cracks may be formed before reaching the peak stress (see Section 4.1). Considering that fired clay is a rather inhomogeneous material – the production process causes microcracks to occur –, the weakest web of the block should be the one triggering failure. Let's assume, this weakest web has a significantly smaller strength than each other web. Now, if failure of the reinforced masonry requires formation of a second crack, the strength increase due to the stiffer bed joint should be even higher than in the first case. Therefore, a stochastic approach was chosen to capture these effects within the model.

Inhomogeneities in the single block are common, affecting the material's strength. On the one hand, the used clay is a natural resource; thus, inclusions may occur in the mixture. On the other hand, the mechanical impact on the blocks during the production process as well as the firing process accompanied by material shrinkage induce microcracks.

Structural inhomogeneities, like microcracks, are the main reason for the fluctuation of the obtained strengths. Each block in the numerical model was subdivided in longitudinal webs and transverse webs. Since cracks inducing failure only occur in the transverse webs, solely the differences between these webs were considered. Thereby, a random strength was allocated to each transverse web, while assuming that each web separately has a homogeneous strength.

Kiefer et al. [27] obtained tensile and compressive strengths from experiments in longitudinal, transversal, and extrusion direction. Therefore, mean values μ and standard deviations s are available, assuming that the strength values are distributed normally. For each transverse web, a value x was randomly generated from a standard normal distribution (see Fig. 9a) with the function `randn()` in the programming language *Julia* [4]. The probability density function of the standard normal distribution ensures the random values to be around the mean value 0. Consider x as kind of a strength modification parameter: if x is lower than 0, the strength is less than the mean value; if x is greater than 0, conversely. This parameter was then used to calculate the tensile and compressive stresses for each direction L, T and Z:

$$\sigma_i = \mu_{\sigma_i} - x \cdot s_{\sigma_i}, \qquad (29)$$

with the mean value μ_{σ_i} and standard deviation s_{σ_i} of the treated strength σ_i (see Fig. 9b). The obtained values were further used to calculate the shear strengths according to Eq. (21).

During cracking processes in a system, energy is released. Since the damage evolution depends on the critical energy release rate, the strength fluctuation due to existing microcracks has to be considered there. The entirely undamaged material with a failure stress $\sigma_{f,max}$ has a critical energy release rate $G_{c,max}$. At the mean failure stress μ_{σ_f}, the critical energy release rate results in μ_{G_c}, which is defined by the values $G_{c,I}$ to $G_{c,III}$ for each failure mode in Section 2.2.2. Since the production-related damage and, therefore, the failure stress σ_f varies with each transverse web, the related critical energy release rate G_c^* has to deviate from the mean value by ΔG:

$$G_c^* = \mu_{G_c} - \Delta G. \qquad (30)$$

Note, that the difference ΔG may be negative in case of a web, being stronger than the average. Griffith [20] proposed a way to calculate the critical stress as follows:

$$\sigma_f = \sqrt{\frac{G_c \cdot E}{\pi \cdot a}}, \qquad (31)$$

with the material's Young's modulus E and the crack length a. Comparing the deviating failure stress σ_f^* to the mean failure stress μ_{σ_f} in terms of Griffith's formulation yields to an equation for the adapted critical energy release rate G_c^* (see Fig. 10):

$$\frac{\mu_{\sigma_f}}{\sigma_f^*} = \sqrt{\frac{\mu_{G_c}}{G_c^*}} \qquad \rightarrow \qquad G_c^* = \mu_{G_c} \cdot \frac{\sigma_f^{*2}}{\mu_{\sigma_f}^2}. \qquad (32)$$

2.6. Validating the strategies

Trinko et al. [50] investigated the effect of fibre reinforced bed joints on the vertical compressive strength of brick masonry in experiments on solid brick pillars (see Fig. 11). Therefore, he tested three pillars without reinforcement and another three pillars, reinforced with a glass fibre
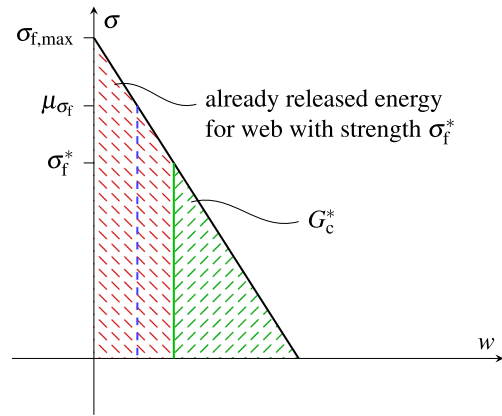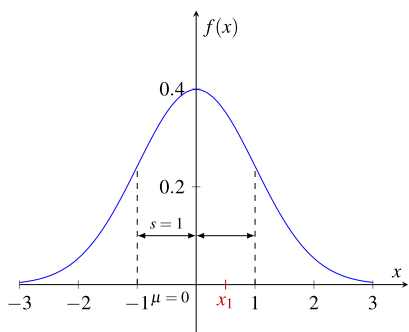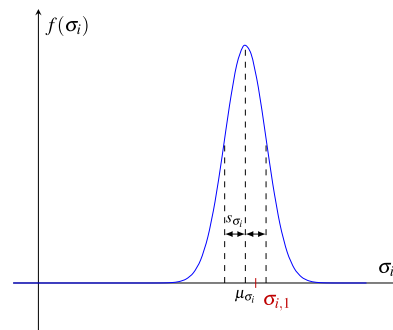
Fig. 10. The critical energy release rate is reduced due to production-related damage.

(a) The value x_1 is randomly picked from a standard normal distribution.

(b) With a given mean value μ_{σ_i} and standard deviation s_{σ_i} the randomly picked strength $\sigma_{i,1}$ can be calculated.

Fig. 9. Standard normal distribution (a) and normal distribution of material strength σ_i (b).
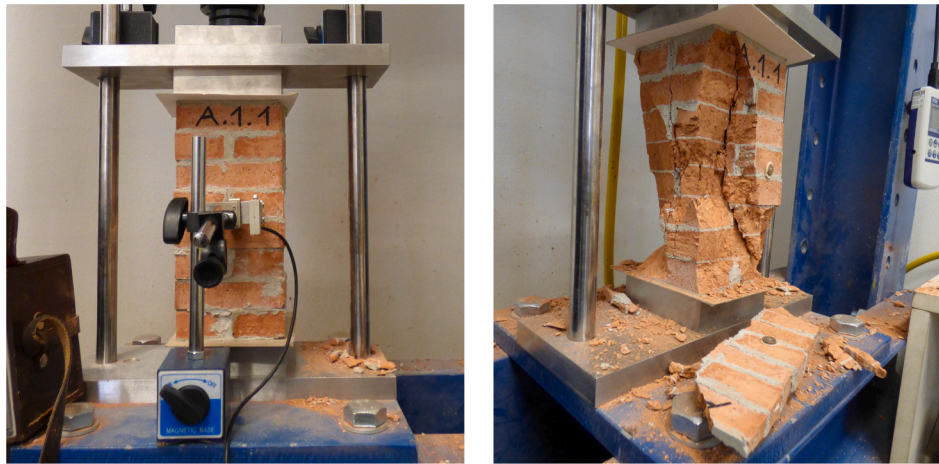
Fig. 11. Solid brick pillar without reinforcement, before and after the experiment [50].

mesh, as it is typically used for plastering facades. He considered pillars with a square cross section and eight layers, consisting of Austrian standard sized bricks reduced to 40% of their original size. Hence, the pillars were 10 cm wide and 22.2 cm high, with a 2 mm mortar joint between each layer of bricks. Those masonry specimens were modelled with the previously described simulation strategies (Sections 2.1,2.5) in order to verify the proposed numerical model, which was then used to estimate the effect of a reinforced mortar bed joint on the compressive strength of vertically perforated clay blocks. Kiefer et al. [27] already validated the model for the compressive strength of unreinforced clay block masonry by an extensive set of experiments. Therefore, the focus lies in the validation of the modelling strategies cosidering the bed joint reinforcement.

2.6.1. Material parameters

Trinko et al. [50] experimentally obtained most of the material parameters in Tables 2–4 for the used brick and mortar, missing values were predicted by applying ratios between values obtained in literature.

2.6.1.1. Brick. Nine independent parameters, eg. three Young's moduli E_i, three Poisson's ratios ν_{ij}, and three shear moduli G_{ij}, are necessary to fully describe the stiffness tensor of an orthotropic material. Measuring the travel time of ultrasonic longitudinal and transverse waves through a solid specimen for each direction T, T and Z yields six independent components of the stiffness tensor. With the Poisson's ratios of the brick approximated with 0.1 according to the data provided by Hannawald and Brameshuber [23], the Young's moduli and shear moduli could be calculated (see Table 2).

To obtain the compressive strengths, Trinko et al. [50] conducted compression tests in each principal material direction. While the tensile strengths where scaled to the compressive strengths with the ratio given by Kiefer et al. [27], the shear strengths were estimated as mean value of Eq. (21). Table 3 contains all the strength values used for the model.

2.6.1.2. Mortar. Measuring the travel time of ultrasonic transverse and longitudinal waves led Trinko et al. [50] to the stiffness properties of mortar. Since the mortar is supposed to be isotropic, the two

independent measured values suffice to fully describe the stiffness tensor of the mortar.

2.6.1.3. Glass fibre mesh and reinforced mortar. Synthetically coated glass fibres form the orthogonally organized mesh, with a mesh width of 4 mm, which was embedded in the bed joint of the pillars. Since the fibre strands consist of numerous fine glass fibres, the cross section of the strands may vary over the mesh. Therefore, a reliable way to estimate the volume fraction of the glass fibres is found over the areal weight of the mesh. Hence, dividing the areal weight m by the mass density ρ_f times the bed joint thickness d_m times two (for considering only fibres oriented in the same direction), results in the volume fractions in directions x and y, $f_{f,x}$ and $f_{f,y}$, respectively:

$$f_{f,x} = f_{f,y} = \frac{m}{2 \cdot \rho_f \cdot d_m} = \frac{0,0145 \text{ g/cm}^2}{2 \cdot 2.5 \text{g/cm}^3 \cdot 0.2 \text{ cm}} = 1,45\%. \tag{33}$$

Applying the homogenization scheme presented in Section 2.3.1 on the mortar properties in Table 4, the glass fibre properties in Table 1 and the volume fractions in Eq. (33) yields the homogenized stiffness of the reinforced mortar. Thereby, the components C_{xxxx} and C_{yyyy} of the stiffness tensor, which have a strong influence on the lateral stresses triggering failure, increase around 13%.

2.6.2. Experimental results

Trinko et al. [50] obtained failure loads for each specimen and divided them by their cross section to receive the vertical compressive masonry strengths in Table 5. While the mean value of the masonry strength increased by 15.38% when reinforcing the mortar bed joint, the standard deviation of the results decreased significantly. Additionally, [50] observed a main difference in the failure mechanism: While the specimens *without reinforcement* failed brittle, immediately after the first crack occurred, the *reinforced* specimens allowed the loading to be increased further, even after the first crack. Hence, the reinforced mortar joints caused a more ductile damage evolution behaviour.

Table 2
Orthotropic elastic properties for solid bricks [50].

Young's modulus (MPa)			Poisson's ratio			Shear modulus (MPa)		
E_{LL}	E_{TT}	E_{ZZ}	ν_{TZ}	ν_{ZL}	ν_{LT}	G_{TZ}	G_{ZL}	G_{LT}
9951 ($\pm$898.6)	8670 ($\pm$471.7)	13 500	0.1	0.1	0.1	3774 ($\pm$261.2)	3725 ($\pm$232.3)	2700

Values in parenthesis represent standard deviations.

Table 3

Orthotropic material strengths for solid bricks [50].

Compressive strength (MPa)			Tensile strength (MPa)			Shear strength (MPa)		
$\sigma_{c,L}$	$\sigma_{c,T}$	$\sigma_{c,Z}$	$\sigma_{t,L}$	$\sigma_{t,T}$	$\sigma_{t,Z}$	$\sigma_{s,TZ}$	$\sigma_{s,ZL}$	$\sigma_{s,LT}$
16.42	13.69	21.38	8.04[a]	6.87[a]	9.12[a]	8.38[b]	9.02[b]	7.49[b]
($\pm$1.62)	($\pm$2.56)	($\pm$2.79)						

Values in parenthesis represent standard deviations.

[a] Scaled based on experiments conducted by Kiefer et al. [27].

[b] Mean value of results obtained with Eq. (21).

Table 4

Isotropic elastic properties of the used mortar.

Young's modulus	E	8378 MPa ($\pm$264.93)
Poisson's ratio	ν	0.223 ($\pm$0.00474)

Values in parenthesis represent standard deviations.

Table 5

Vertical compressive strength of the specimen (MPa) [50].

		Series	
		w/o reinforcement	with reinforcement
Test	I	15.08	15.91
	II	11.96	16.39
	III	14.82	16.00
	Mean value	13.95 ($\pm$1.73)	16.10 ($\pm$0.26)
	Increase	–	15,38%

Values in parenthesis represent standard deviations.

2.6.3. Numerical results

Both the unreinforced and reinforced specimen were simulated with the modelling strategies above (except the stochastic allocation of strengths), considering the material parameters in Tables 2–4. The representative unit cell consists of two bricks and two bed joints in height (see Fig. 12). As the solid brick pillars are more than two times higher than wide, a uniaxial stress state can be expected in the middle of the specimen. Hence, the unit cell approach with periodic boundary conditions, which represents an infinitely large pillar in a uniaxial stress state, is suitable for efficiently modelling the considered problem.

When comparing the obtained masonry strengths to each other, the numerical results fit rather accurately to the experimentally found values (see Fig. 13). While the boxes represent the experiments, the crosses mark the numerically obtained strengths. Both models led to results just above the mean value of the experiments, and predicted a strength increase of 13.64% (compared to 15.38% in the experiments). Since tensile failure of the mortar head joints was neglected, an over-estimation of the peak stress seems reasonable. Modelling the pillars without a mortared head joint at all would lead to a lower bound of the peak stress, as comparative calculations showed.
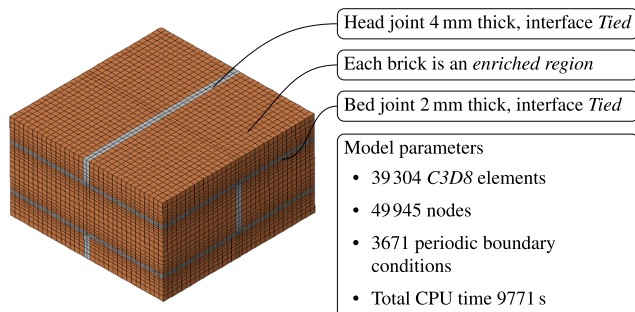

Fig. 12. FE mesh of the solid brick model.

Head joint 4 mm thick, interface *Tied*

Each brick is an *enriched region*

Bed joint 2 mm thick, interface *Tied*

Model parameters
• 39 304 *C3D8* elements
• 49 945 nodes
• 3671 periodic boundary conditions
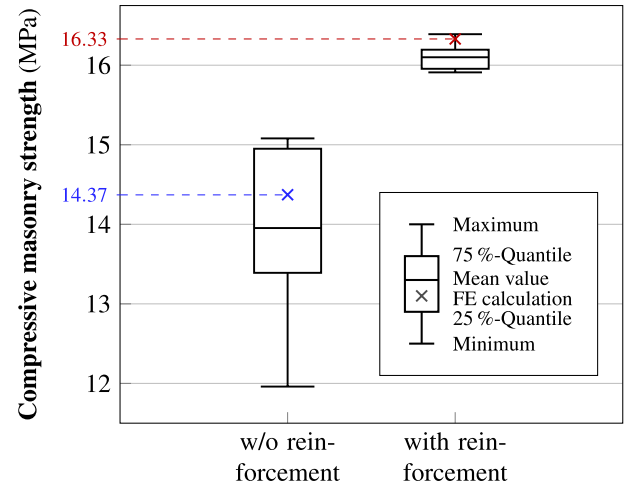• Total CPU time 9771 s

Fig. 13. Numerical results compared to the experimental results.

Additionally, the same mechanism as [50] observed, occurred: While the unreinforced pillar failed immediately after formation of the first crack, the reinforced pillar could bear a load increase, even after the first crack occurred (see Fig. 14). The experiments showed a distinct nonlinear behaviour, due to micro cracks in both brick and mortar as well as the rupture of the head joints. Since solely macro cracks in the brick units were introduced in the model, which are crucial for the magnitude of the peak stress, the numerical simulations followed a linear path until peak stress.

Considering the good agreement of the peak stress values between the simulations and the experiments, the proposed modelling strategies seem to be suitable for application on the block masonry model.
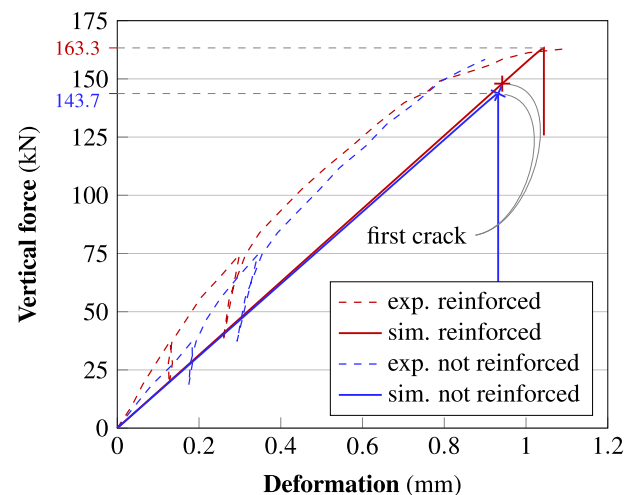

Fig. 14. Load-displacement diagram for simulations and experiments (with and without reinforcement).

3. Compressive strength increase of vertically perforated clay block masonry

In the next step, the validated numerical simulation tool was used to estimate the increase of the vertical compressive strength of vertically perforated clay block masonry due to the use of reinforced bed joints.

3.1. Unit cell

The examined block has a height of 249 mm and a length of 248 mm. Choosing the unit cell one block long and two blocks high and considering a 1 mm thick bed joint, as well as a 1 mm wide horizontal gap between the blocks, the total dimensions of the cell add up to 249 mm length and 500 mm height. Hence, the periodicity vectors $\mathbf{c}_x$ and $\mathbf{c}_z$ are:

$$\mathbf{c}_x = \begin{pmatrix} 249 \\ 0 \\ 0 \end{pmatrix} \text{mm} \quad \text{and} \quad \mathbf{c}_z = \begin{pmatrix} 0 \\ 0 \\ 500 \end{pmatrix} \text{mm}. \tag{34}$$

As perfect offset of half a blocks width is not to be expected on a construction site, the offset was modelled slightly higher, thereby minimizing the contact area. Hence, compressive stresses are directly transferred between the longitudinal webs, but not between the transversal webs. Since the mortar layer over the vertical shafts and transversal webs was supposed to be damaged due to shrinkage induced cracks, the bed joint was partitioned in two sections (see Fig. 15):

- the uncracked mortar layer above the longitudinal webs of the blocks and
- the cracked mortar layer above the vertical shafts and transversal webs of the blocks.

While the uncracked section was modelled with the properties of the pure mortar or the homogenized properties of the reinforced mortar, the cracked part wasn't modelled at all in the unreinforced model. However, the properties of the glass fibre mesh were considered there in the model with reinforcement. Fig. 16 shows the FE mesh of the modelled unit cell. The transversal webs were defined as *enriched regions*, thus regions where nodal degrees of freedom are enriched. The simulations were run on a high performance computing cluster, using eight CPU cores in parallel per model. Therefore, the calculations took approximately 4 hours on average.

3.2. Brick

Nine independent parameters, more precisely the Young's moduli E_{LL}, E_{TT}, E_{ZZ}, the Poisson's ratios ν_{LT}, ν_{TZ}, ν_{ZL}, and the shear moduli G_{LT}, G_{TZ}, G_{ZL}, were used to define the stiffness properties of the used clay (see Table 6). Kiefer et al. [27] obtained values for E_{ZZ} in experiments on comparable blocks and took them as a basis for calculating the
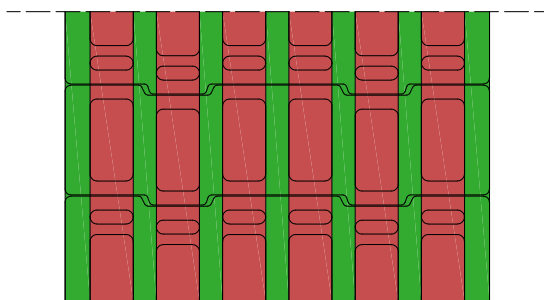

Fig. 15. Partitioning of the bed joint in two sections: uncracked (green) and cracked (red). The black lines represent the outline of the blocks directly below and above the bed joint. (For interpretation of the references to color in this figure legend, the reader is referred to the web version of this article.)

remaining Young's moduli and shear moduli, with the ratios from Bourret et al. [7] as well as Hannawald and Brameshuber [23]. As before, the Poisson's ratios were estimated with the experimentally obtained data from [23].

For the strength properties Kiefer et al. [27] referred to an extensive series of compressive and bending tensile tests of a comparable block (see Table 7). The shear strengths were estimated as the mean values of the results, obtained in Eq. (21).

3.3. Mortar

Compressive failure of the mortar bed joint is not considered as relevant for the given loading scenario. In the absence of experimental data, Kiefer et al. [27] estimated the elastic properties considering the findings of Vekey [51] as well as Sarhosis and Sheng [47] (see Table 8).

While the elastic properties of the uncracked reinforced mortar were homogenized by means of the homogenization scheme presented in Section 2.3.1, solely the properties of the fibre mesh were considered in the cracked regions (see Table 9). To avoid numerical problems due to changing thickness of the mortar layer, the fibre stiffness was converted to an effective stiffness over the thickness of the mortar layer. Therefore, the lateral Young's moduli were obtained by multiplying the fibre's Young's modulus E_f with the volume fraction in the particular direction, $f_{f,i}$. Since the shear stiffness of the mesh is rather small, compared to the Young's modulus, the shear moduli and Poisson's ratio were set to nearly zero.

3.4. Numerical approaches

3.4.1. Fixed strength values
For developing a relationship between the volume fraction of the reinforcing mesh and the compressive masonry strength, at first 25 models with different volume fractions were simulated. Hereby, the volume fraction of the glass fibres was increased in steps of 0.25%, starting at 0% until reaching 6%. The allocated strengths for these models were fixed to the mean values, given in Table 7.

3.4.2. Stochastic allocated strength values
For the stochastic approach, ten models with different strength allocations were randomly generated. Thereby, random strength properties were assigned to each transversal web according to Section 2.5. Each model was simulated in three different states: without reinforcement, reinforced with $f_{f,y} = 3\%$, and reinforced with $f_{f,y} = 6\%$. Therefore, 30 models were simulated in total, the results were statistically evaluated afterwards.

4. Results and discussion

4.1. Fixed strength simulation

Fig. 17 shows the developed relationship between the volume fraction of the glass fibres and the compressive masonry strength. While the blue curve denotes the calculated compressive masonry strength, the red dashed curve defines the average compressive stress when the first crack occurred in the model. Thus, the average compressive stress when the first crack occurs increases linearly, which confirms the assumption of decreasing lateral stresses with increasing mortar stiffness. After the first crack occurrence, the models behave differently with varying volume fraction. Until a volume fraction of $f_{f,y} = 1.75\%$, the numerical models failed immediately after the first crack occurred. With higher amounts of reinforcement, the applied load could be increased beyond the first crack loading. Detailed examination of the resulting crack patterns revealed that, with the volume fraction exceeding 2%, the first crack was being held together by the stiffer bed joint. Additionally, the load could be increased, until a second transverse web failed (see Fig. 18). Therefore, the reinforced bed joint caused the lateral tensile stresses to
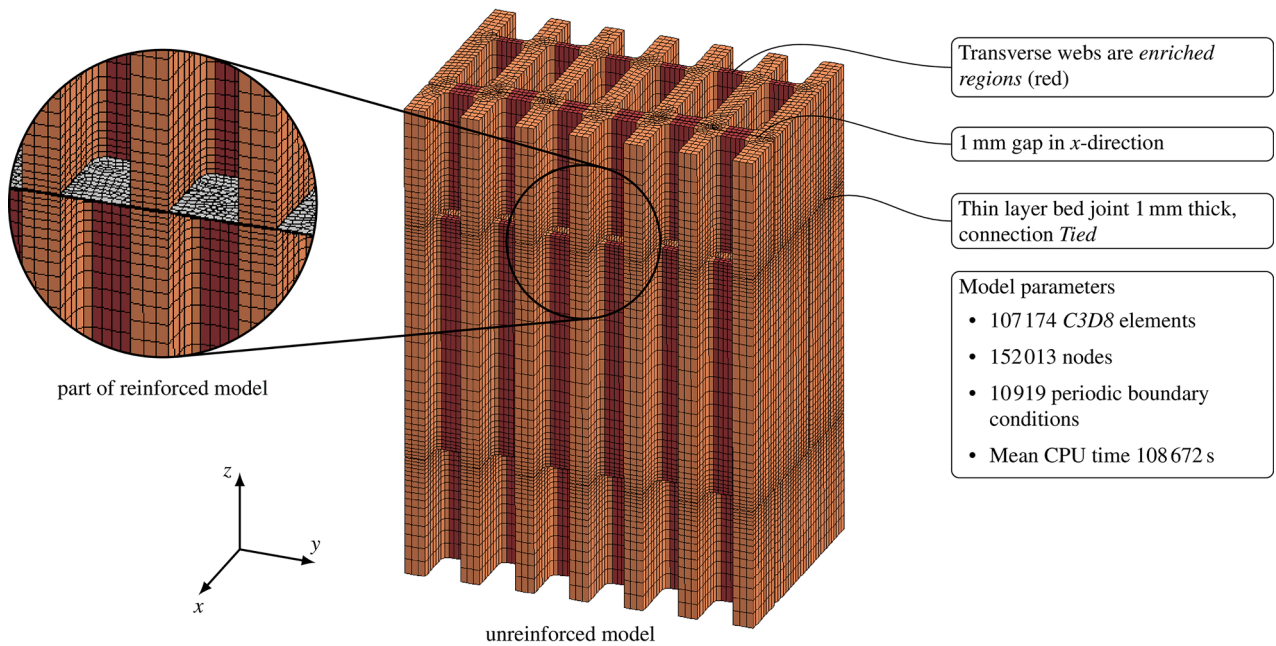
Fig. 16. FE mesh of the unreinforced model and part of the reinforced model.

Table 6
Applied transversally isotropic, elastic properties of the vertically perforated clay blocks [27].

Young's modulus (MPa)			Poisson's ratio			Shear modulus (MPa)		
E_{LL}	E_{TT}	E_{ZZ}	ν_{TZ}	ν_{ZL}	ν_{LT}	G_{TZ}	G_{ZL}	G_{LT}
8738	8738	11 970 (±465)	0.1	0.1	0.1	5509	5509	3972

Values in parenthesis represent the standard deviation.

Table 7
Applied orthotropic strength properties of the vertically perforated clay blocks [27].

Compressive strength (MPa)			Tensile strength (MPa)			Shear strength (MPa)		
$\sigma_{c,L}$	$\sigma_{c,T}$	$\sigma_{c,Z}$	$\sigma_{t,L}$	$\sigma_{t,T}$	$\sigma_{t,Z}$	$\sigma_{s,TZ}$	$\sigma_{s,ZL}$	$\sigma_{s,LT}$
20.8[a]	15.0[a]	21.8 (±1.15)	8.2[a]	7.0[a]	9.3[a]	8.675[b]	9.7[b]	8.275[b]

Values in parenthesis represent the standard deviation.
[a] Scaled with ratios, obtained in other experiments (see [27]).
[b] Mean value of results obtained with Eq. (21).

Table 8
Applied isotropic, elastic properties of the thin bed mortar [27].

Young's modulus	E	5000 MPa
Poisson's ratio	ν	0.2

Table 9
Applied elastic properties of the reinforced mortar joint between the longitudinal webs

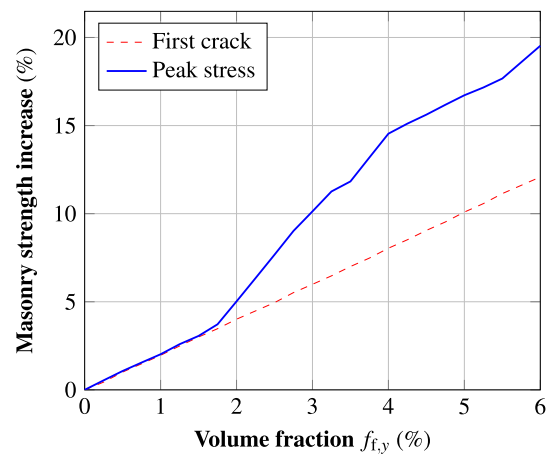| Young's modulus (MPa)			Poisson's ratio			Shear modulus (MPa)		
E_{xx}	E_{yy}	E_{zz}	ν_{yz}	ν_{zx}	ν_{xy}	G_{yz}	G_{zx}	G_{xy}
$E_f \cdot f_{f,x}$	$E_f \cdot f_{f,y}$	5000	0.001	0.001	0.001	10	10	10

Fig. 17. Effect of the glass fibre reinforcement on the vertical compressive masonry strength.

distribute more evenly over the block profile.

Comparing the failure mechanisms observed, this is in accordance to Kiefer et al. [27], who showed that the used approach not only serves an accurate prediction of the compressive masonry strength, but also allows to identify the failure mechanism of vertically perforated block masonry: a spalling of the outer longitudinal webs, due to tensile failure of the transverse webs behind.

When a crack forms in the model without reinforcement, the released tensile stresses redistribute mainly to the crack tip, which is why the crack propagates fast. In the reinforced models, the glass fibre mesh takes most of the released stresses; crack propagation is therefore suspended. Nevertheless, the failure mechanism stayed the same.

At the highest modelled volume fraction, the reinforced bed joint enabled a total masonry strength increase of 19.5%.

4.2. Random strength simulation

The location of the first crack could be predicted in the first approach: due to the homogeneous strengths, the web being subject to
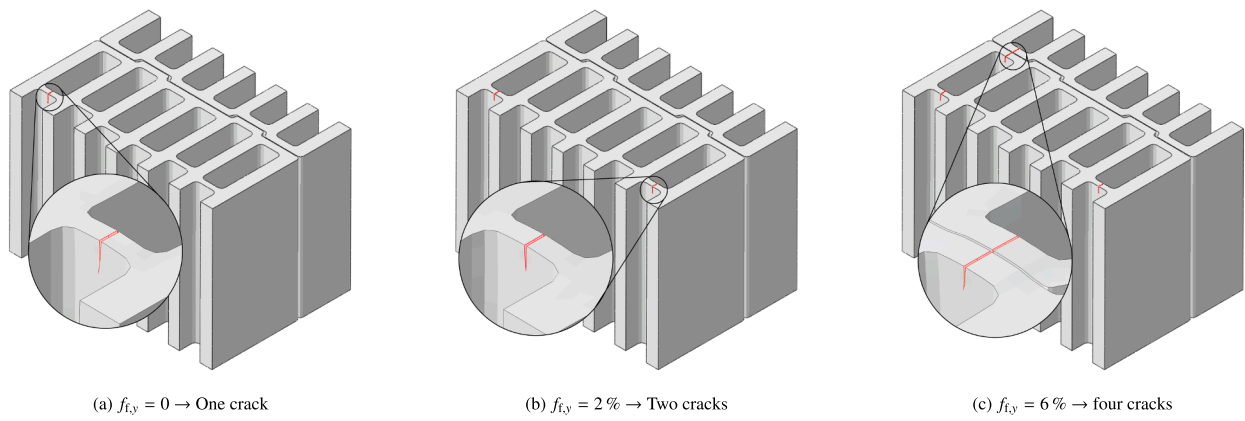
(a) $f_{f,y} = 0 \rightarrow$ One crack

(b) $f_{f,y} = 2\% \rightarrow$ Two cracks

(c) $f_{f,y} = 6\% \rightarrow$ four cracks

Fig. 18. Comparison of the crack pattern at peak stress with different volume fractions $f_{f,y}$. The asymmetric crack pattern originates in asymmetries of the mesh.

the greatest tensile stresses is expected to tear apart first. Taking a closer look at the distribution of longitudinal stresses σ_L, the outer webs turn out to be the ones with the highest stresses. Considering the randomly allocated web strengths, such a prediction cannot be made anymore. The results showed that if there was an extremely weak web in the middle of the block, the first crack occurred there (see Fig. 19). Interestingly, in cases where the firstly torn web was not one of the outer webs, the loading could be increased after the first crack, even without reinforcement. In each of the ten models, the compressive masonry strength was not reached until at least one of the outer webs contained a crack. Hence, the failure mechanism of the models amounted to the familiar mechanism of vertically perforated block masonry: a spalling of the outer shell.

The randomly generated models consisted of webs with lower strengths than the mean values as well as webs with higher strengths. Therefore, on average the mean clay strength over a individual model

amounted to approximately the mean strengths in Table 7. However, each of the randomly generated models led to a lower compressive masonry strength than with the homogeneously allocated strengths. This illustrates that the webs with strengths below average have a greater effect on the compressive strength than the stronger ones, even though the weakest web alone is not decisive for structural failure.

Fig. 20 shows the increase of the compressive masonry strength with the volume fraction. Since the strength increase of each individual model more or less doubled when changing the volume fraction from 3% to 6%, the standard deviation changed in the same manner. The mean value of the strength increase at the highest modelled volume fraction amounted to 28.87%.

Even though the obtained masonry strengths were consistently lower in the randomly generated models, the mean strength increase exceeded the aforementioned by 9%.

Fig. 21 shows the obtained results with the stochastic simulation approach without reinforcement (right box) in comparison to compressive tests on RILEM samples, using the examined block geometry (left box). While Kiefer et al. [27] accomplished to estimate the compressive strength within the fluctuation of the test results (red cross), the stochastic approach reproduces even these fluctuations pretty accurately. The simulated mean value is nearly the same as the mean value obtained in experiments.
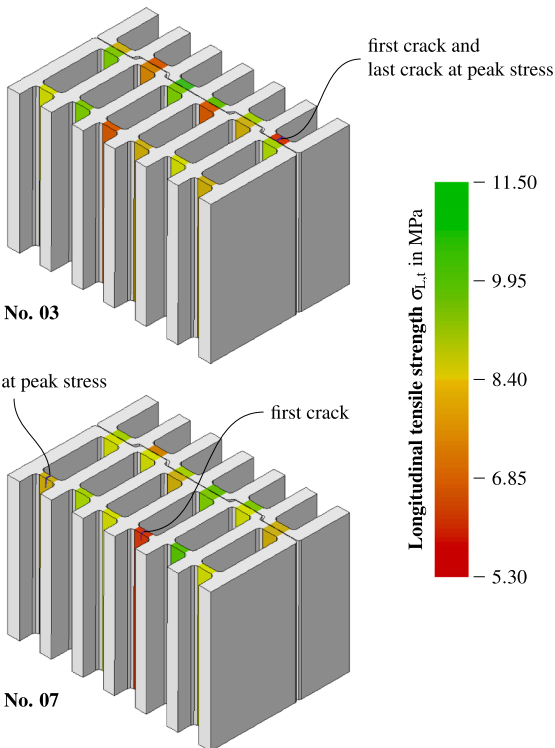
4.3. Feasible volume fraction

Regarding the maximum feasible volume fraction of reinforcement within the bed joint, one can consider the aforementioned separation of
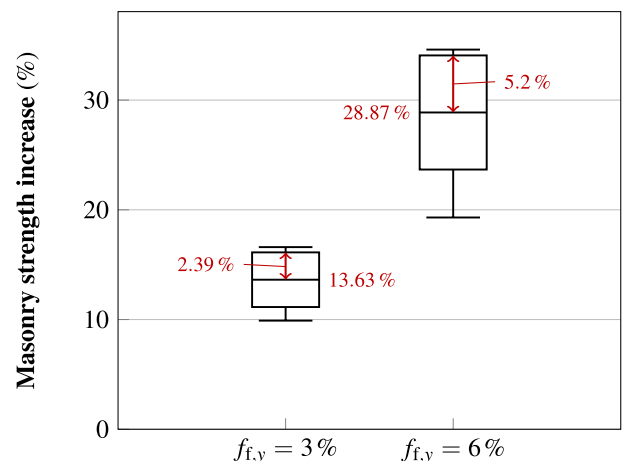

Fig. 19. Comparison of the crack pattern at peak stress with different strength allocations on unreinforced models.

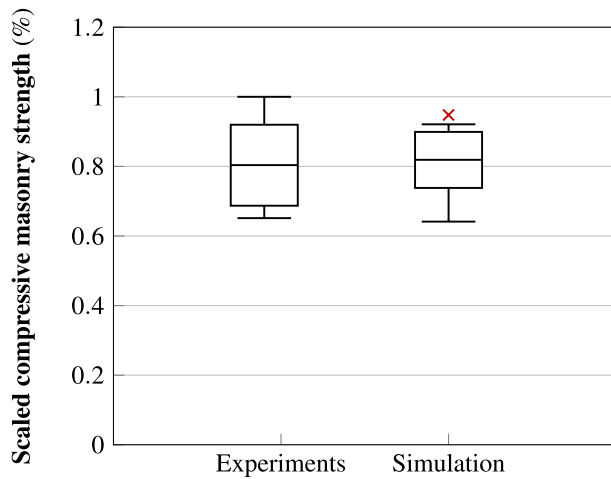**Fig. 20.** Statistical evaluation of the strength increase.

Fig. 21. Compressive strengths obtained in experiments on RILEM samples (left box) compared to results using the stochastic simulation approach (right box) and the results according to Kiefer et al. [27] (marked with ×). The strength values are scaled to the maximum strength obtained in the experiments.

Table 10
Comparison of the fixed value and random value strength increase.

	Volume fraction $f_{f,y}$ (%)		
	0	3.0	6.0
Fixed values			
increase	–	10.1	19.5
Statistically allocated values			
Mean value increase	–	13.63	28.87
5%-quantile increase	–	15.28	33.81

scales (see Eq. (23)). Assuming perfectly round fibre strands with a diameter of $1/\alpha$ times the joint thickness, in a orthogonally arranged mesh with a constant mesh width of β times the strand diameter, the volume fraction can be calculated as follows:

$$f_{f,y} = \frac{A_{\text{fibre}}}{A_{\text{joint}}} = \frac{\frac{d^2\pi}{4}\cdot\frac{l}{a}}{l\cdot h} = \frac{\frac{h^2\pi}{\alpha^2\cdot4}\cdot\frac{l}{\beta\cdot h}}{l\cdot h} = \frac{\pi}{4\cdot\alpha^2\cdot\beta}. \tag{35}$$

Considering the generally acknowledged values for the separation of scales, α should be at least 1.5 to 3 [13,44]. Additionally, the mesh width should be great enough, not to separate the mortar joint into two layers. Hence, a mesh width three times greater than the fibre strand diameter, seems to be reasonable. Using 2 for α and 3 for β in Eq. (35), the maximum volume fraction results in 6.54%.

Concludingly, the simulated volume fraction of 6% seems to be reasonably attainable with an embedded glass fibre mesh. Therefore, the 5%-quantile of the compressive masonry strength could reach an increase of over 33% (see Table 10).

5. Conclusion

Within the present work, a numerical approach for estimating the effect of glass fibre reinforced bed joints on the vertical compressive strength of vertically perforated clay block masonry was developed. Based on the presented research, the following conclusions could be drawn:

- Glass fibre reinforced bed joints enable a significant increase of the vertical compressive strength of perforated clay block masonry. The compressive masonry strength increase can be split up into two mechanisms:

    the *first crack occuring at a higher load*, due to the decrease of lateral tensile stresses, and
    the *onset of cracking arising at a higher load*, as the fibre mesh bridges the open crack.
- The reinforcement within the mortar layer prevents the outer shell from spalling, after the first cracks occur, thereby yielding a more ductile damage behaviour.
- Weaker webs within the block affect the vertical compressive strength, which is why the approach from Kiefer et al. [27] tended to overestimate the test results. Nevertheless, considering the fluctuation of test results and the high effort for stochastic calculations, their approach seems to be sufficient to reasonably estimate masonry strengths.

Besides numerous advantages of glass fibre reinforced bed joints (such as the increase of ductility, weather protection during construction, or a continuous mortar layer), the conducted simulations reveal the potential of bed joint reinforcement in raising the compressive masonry strength. While the potential for optimization is exhausted in modifying the block geometry, bed joint reinforcement could be a possible approach for increasing the masonry strength further. Even for already existing block geometries, the approach could enable a significantly higher vertical compressive strength with relatively low effort. Thereby, it is necessary to emphasize that the presented compressive strength increase of vertical perforated clay blocks originates in numerical simulations with complex modelling strategies, which were solely validated by experiments on solid brick masonry pillars. Hence, for checking the significance of this results, a series of experiments on vertically perforated clay block masonry is necessary.

By use of the presented unit cell approach, arbitrary loading states on masonry walls can be investigated apart from uniaxial compression. Therefore, the effect of a reinforced bed joint on the load carrying capacity in shear or bending scenarios could be estimated. For these reasons, the presented approach constitutes a significant contribution to the potential assessment of fibre reinforced bed joints.

CRediT authorship contribution statement

Raphael Suda: Conceptualization, Methodology, Software, Formal analysis, Investigation, Writing - original draft, Visualization. **Thomas Kiefer:** Methodology, Software, Writing - review & editing. **Christian Schranz:** Writing - review & editing. **Josef Füssl:** Writing - review & editing, Supervision, Project administration, Funding acquisition.

Declaration of Competing Interest

The authors declare that they have no known competing financial interests or personal relationships that could have appeared to influence the work reported in this paper.

Acknowledgements

References

[1] Anthoine A, Pegon P. Numerical analysis and modelling of the damage and softening of brick masonry. Netherlands, Dordrecht: Springer; 1996. p. 152–84. https://doi.org/10.1007/978-94-011-0603-0_7.
[2] Belytschko T, Black T. Elastic crack growth in finite elements with minimal remeshing. Int J Numer Meth Eng 1999;45:601–20. https://doi.org/10.1002/(SICI)1097-0207(19990620)45:5<601::AID-NME598>3.0.CO;2-S.

[3] Bertolesi E, Milani G, Fagone M, Rotunno T, Grande E. Heterogeneous FE model for single lap shear tests on FRP reinforced masonry curved pillars with spike anchors. Constr Build Mater 2020;258:119629. https://doi.org/10.1016/j.conbuildmat.2020.119629.

[4] Bezanson J, Edelman A, Karpinski S, Shah VB. Julia: A fresh approach to numerical computing. SIAM Rev 2017;59:65–98. https://doi.org/10.1137/141000671.

[5] Böhm HJ. A short introduction to basic aspects of continuum micromechanics. ILSB-Arbeitsbericht 2016; 2016. https://www.ilsb.tuwien.ac.at/links/downloads/ilsbrep206.pdf.

[6] Bocca P, Carpinteri A, Valente S. Fracture mechanics of brick masonry: size effects and snap-back analysis. Mater Struct 1989;22:364–73. https://doi.org/10.1007/bf02472507.

[7] Bourret J, Tessier-Doyen N, Guinebretiere R, Joussein E, Smith DS. Anisotropy of thermal conductivity and elastic properties of extruded clay-based materials: Evolution with thermal treatment. Appl Clay Sci 2015;116–117:150–7. https://doi.org/10.1016/j.clay.2015.08.006.

[8] Bruggi M, Taliercio A. Design of masonry blocks with enhanced thermomechanical performances by topology optimization. Constr Build Mater 2013;48:424–33. https://doi.org/10.1016/j.conbuildmat.2013.07.023.

[9] Coz Díaz J, Nieto PG, Rabanal FÁ, Martínez-Luengas AL. Design and shape optimization of a new type of hollow concrete masonry block using the finite element method. Eng Struct 2011;33:1–9. https://doi.org/10.1016/j.engstruct.2010.09.012.

[10] DIN 4108-7. Wärmeschutz und Energie-Einsparung in Gebäuden - Teil 7: Luftdichtheit von Gebäuden - Anforderungen, Planungs- und Ausführungsempfehlungen sowie -beispiele. Standard. DIN Deutsches Institut für Normung e. V.. Berlin, GER; 2011.

[11] Ding J, Yu T, Yang Y, Bui TQ. An efficient variable-node XFEM for modeling multiple crack growth: A Matlab object-oriented implementation. Adv Eng Softw 2020;140:102750. https://doi.org/10.1016/j.advengsoft.2019.102750.

[12] Doan DH, Bui TQ, Do TV, Duc ND. A rate-dependent hybrid phase field model for dynamic crack propagation. J Appl Phys 2017;122:115102. https://doi.org/10.1063/1.4990073.

[13] Drugan WJ, Willis JR. A micromechanics-based nonlocal constitutive equation and estimates of representative volume element size for elastic composites. J Mech Phys Solids 1996;44:497–524. https://doi.org/10.1016/0022-5096(96)00007-5.

[14] Eis A, Vassilev T. Übersicht über abgeschlossene und laufende Forschungsvorhaben im Mauerwerksbau. In: Mauerwerk-Kalender 2012. Wiley-VCH Verlag GmbH & Co. KGaA; 2013. p. 609–47. doi: 10.1002/9783433601617.ch17.

[15] EN 1052-1. Methods of test for masonry - Part 1: Determination of compressive strength. Standard. Brussels: BEL; 1998.

[16] Eshelby JD. The determination of the elastic field of an ellipsoidal inclusion, and related problems. Proc Roy Soc Math Phys Eng Sci 1957;241:376–96. https://doi.org/10.1098/rspa.1957.0133.

[17] Fu SY, Lauke B, Mäder E, Yue CY, Hu X. Tensile properties of short-glass-fiber- and short-carbon-fiber-reinforced polypropylene composites. Compos A: Appl Sci Manuf 2000;31:1117–25. https://doi.org/10.1016/s1359-835x(00)00068-3.

[18] Graubner CA, Richter L. Diskrete FE-Modellierung von Mauerwerk zur Bestimmung der Druckfestigkeit. Mauerwerk 2007;11(6):342–8. https://doi.org/10.1002/dama.200700354.

[19] Gravouil A, Moës N, Belytschko T. Non-planar 3d crack growth by the extended finite element and level sets–Part II: Level set update. Int J Numer Meth Eng 2002; 53(11):2569–86. https://doi.org/10.1002/nme.430.

[20] Griffith AA. The phenomena of rupture and flow in solids. Philos Trans Roy Soc Math Phys Engi Sci 1921;221:163–98.

[21] Grillanda N, Valente M, Milani G, Chiozzi A, Tralli A. Advanced numerical strategies for seismic assessment of historical masonry aggregates. Eng Struct 2020; 212:110441. https://doi.org/10.1016/j.engstruct.2020.110441.

[22] Hannawald J. Determining the tensile softening diagram of concrete-like materials using hybrid optimisation. In: Measuring, Monitoring and Modeling Concrete Properties. Netherlands: Springer; 2006. p. 179–87. https://doi.org/10.1007/978-1-4020-5104-3_22.

[23] Hannawald J, Brameshuber W. Ermittlung effektiver elastischer Eigenschaften von Hochlochziegeln mittels numerischer Simulation. Mauerwerk 2007;11(6):330–4. https://doi.org/10.1002/dama.200700352.

[24] Hoffman O. The brittle strength of orthotropic materials. J Compos Mater 1967;1 (2):200–6. https://doi.org/10.1177/002199836700100210.

[25] Holbery J, Houston D. Natural-fiber-reinforced polymer composites in automotive applications. JOM 2006;58:80–6. https://doi.org/10.1007/s11837-006-0234-2.

[26] Jasiński R, Drobiec Ł. Study of Autoclaved Aerated Concrete Masonry Walls with Horizontal Reinforcement under Compression and Shear. Procedia Eng 2016;161: 918–24. https://doi.org/10.1016/j.proeng.2016.08.758.

[27] Kiefer T, Kariem H, Lukacevic M, Füssl J. The compressive strength of vertically perforated clay block masonry predicted by means of a unit-cell type numerical simulation tool taking discrete cracking into account. Constr Build Mater 2017; 150:24–34. https://doi.org/10.1016/j.conbuildmat.2017.05.201.

[28] Kohlhauser C, Hellmich C. Ultrasonic contact pulse transmission for elastic wave velocity and stiffness determination: Influence of specimen geometry and porosity. Eng Struct 2013;47:115–33. https://doi.org/10.1016/j.engstruct.2012.10.027.

[29] Laws N. The determination of stress and strain concentrations at an ellipsoidal inclusion in an anisotropic material. J Elast 1977;7(1):91–7. https://doi.org/10.1007/bf00041133.

[30] Leonetti L, Greco F, Trovalusci P, Luciano R, Masiani R. A multiscale damage analysis of periodic composites using a couple-stress/cauchy multidomain model: Application to masonry structures. Compos B: Eng 2018;141:50–9. https://doi.org/10.1016/j.compositesb.2017.12.025.

[31] Lourenço PB. Computational Strategies for Masonry Structures. Ph.D. thesis. Delft University of Technology; 1996.

[32] Marigo JJ, Maurini C, Pham K. An overview of the modelling of fracture by gradient damage models. Meccanica 2016;51:3107–28. https://doi.org/10.1007/s11012-016-0538-4.

[33] Melenk JM, Babuška I. The partition of unity finite element method: basic theory and applications. Comput Methods Appl Mech Eng 1996;139(1–4):289–314. https://doi.org/10.1016/S0045-7825(96)01087-0.

[34] Mendes N, Zanotti S, Lemos JV. Seismic Performance of Historical Buildings Based on Discrete Element Method: An Adobe Church. J Earthquake Eng 2018:1–20. https://doi.org/10.1080/13632469.2018.1463879.

[35] Messali F, Esposito R, Ravenshorst GJP, Rots JG. Experimental investigation of the in-plane cyclic behaviour of calcium silicate brick masonry walls. Bull Earthq Eng 2020;18:3963–94. https://doi.org/10.1007/s10518-020-00835-x.

[36] Michel JC, Moulinec H, Suquet P. Effective properties of composite materials with periodic microstructure: a computational approach. Comput Methods Appl Mech Eng 1999;172(1–4):109–43. https://doi.org/10.1016/s0045-7825(98)00227-8.

[37] Miehe C, Hofacker M, Welschinger F. A phase field model for rate-independent crack propagation: Robust algorithmic implementation based on operator splits. Comput Methods Appl Mech Eng 2010;199:2765–78. https://doi.org/10.1016/j.cma.2010.04.011. https://www.sciencedirect.com/science/article/pii/S0045782510001283.

[38] Moës N, Gravouil A, Belytschko T. Non-planar 3d crack growth by the extended finite element and level sets – Part I: Mechanical model. Int J Numer Meth Eng 2002;53(11):2549–68. https://doi.org/10.1002/nme.429.

[39] Moradabadi E, Laefer DF, Clarke JA, Lourenço PB. A semi-random field finite element method to predict the maximum eccentric compressive load for masonry prisms. Constr Build Mater 2015;77:489–500. https://doi.org/10.1016/j.conbuildmat.2014.12.027.

[40] Mori T, Tanaka K. Average stress in matrix and average elastic energy of materials with misfitting inclusions. Acta Metall 1973;21:571–4. https://doi.org/10.1016/0001-6160(73)90064-3.

[41] Nagy B. Numerical geometry optimization and modelling of insulation filled masonry blocks. In: Proceedings of the 1st International Conference on Numerical Modelling in Engineering. Springer Singapore; 2018. p. 1–13. doi: 10.1007/978-981-13-2405-5_1.

[42] Najafgholipour MA, Maheri MR, Lourenço PB. Capacity interaction in brick masonry under simultaneous in-plane and out-of-plane loads. Constr Build Mater 2013;38:619–26. https://doi.org/10.1016/j.conbuildmat.2012.08.032.

[43] Nguyen THA, Bui TQ, Hirose S. Smoothing gradient damage model with evolving anisotropic nonlocal interactions tailored to low-order finite elements. Comput Methods Appl Mech Eng 2018;328:498–541. https://doi.org/10.1016/j.cma.2017.09.019.

[44] Pensée V, He QC. Generalized self-consistent estimation of the apparent isotropic elastic moduli and minimum representative volume element size of heterogeneous media. Int J Solids Struct 2007;44:2225–43. https://doi.org/10.1016/j.ijsolstr.2006.07.003.

[45] Pluijm R. Out-of-plane bending of masonry: behaviour and strength. In: Department of the Built Environment. Technische Universiteit Eindhoven; 1999. https://doi.org/10.6100/IR528212.

[46] Sadek H, Lissel S. Seismic performance of masonry walls with GFRP and Geogrid Bed joint reinforcement. Constr Build Mater 2013;41:977–89. https://doi.org/10.1016/j.conbuildmat.2012.07.005.

[47] Sarhosis V, Sheng Y. Identification of material parameters for low bond strength masonry. Eng Struct 2014;60:100–10. https://doi.org/10.1016/j.engstruct.2013.12.013.

[48] Scacco J, Ghiassi B, Milani G, Lourenço PB. A fast modeling approach for numerical analysis of unreinforced and FRCM reinforced masonry walls under out-of-plane loading. Compos B: Eng 2020;180:107553. https://doi.org/10.1016/j.compositesb.2019.107553.

[49] Sousa LC, Castro CF, António CC, Sousa H. Topology optimisation of masonry units from the thermal point of view using a genetic algorithm. Constr Build Mater 2011; 25:2254–62. https://doi.org/10.1016/j.conbuildmat.2010.11.010.

[50] Trinko A, Schranz C, Pech A. Tragfähigkeitserhöhung bei Mauerwerk durch textilglasgitterverstärkte Mörtelfugen (english: Increase of the vertical load carrying capacity of masonry due to mortar bed joints with textile glass mesh reinforcement). Mauerwerk 2020;24:72–80. https://doi.org/10.1002/dama.201900019.

[51] Vekey B. Masonry: brickwork, blockwork and stonework. In: Construction Materials: Their Nature and Behaviour, 4th ed. CRC Press; 2010. p. 247–304.

[52] Wen L, Tian R. Improved XFEM: Accurate and robust dynamic crack growth simulation. Comput Methods Appl Mech Eng 2016;308:256–85. https://doi.org/10.1016/j.cma.2016.05.013.

[53] Yu T, Bui TQ. Numerical simulation of 2-D weak and strong discontinuities by a novel approach based on XFEM with local mesh refinement. Comput Struct 2018; 196:112–33. https://doi.org/10.1016/j.compstruc.2017.11.007.